

Robotic modeling of snake traversing large, smooth obstacles reveals stability benefits of body compliance

Qiyuan Fu, Chen Li*

Department of Mechanical Engineering, Johns Hopkins University, Baltimore, Maryland, USA

*Corresponding author. E-mail: chen.li@jhu.edu

Keywords: locomotion, complex terrain, terradynamics, contact, deformation, robophysics

Abstract

Snakes can move through almost any terrain. Although their locomotion on flat surfaces using planar gaits is inherently stable, when snakes deform their body out of plane to traverse complex terrain, maintaining stability becomes a challenge. On trees and desert dunes, snakes grip branches or brace against depressed sand for stability. However, how they stably surmount obstacles like boulders too large and smooth to gain such “anchor points” is less understood. Similarly, snake robots are challenged to stably traverse large, smooth obstacles for search and rescue and building inspection. Our recent study discovered that snakes combine body lateral undulation and cantilevering to stably traverse large steps. Here, we developed a snake robot with this gait and snake-like anisotropic friction and used it as a physical model to understand stability principles. The robot traversed steps as high as a third of its body length rapidly and stably. However, on higher steps, it was more likely to fail due to more frequent rolling and flipping over, which was absent in the snake with a compliant body. Adding body compliance reduced the robot’s roll instability by statistically improving surface contact, without reducing speed. Besides advancing understanding of snake locomotion, our robot achieved high traversal speed surpassing most previous snake robots and approaching snakes, while maintaining high traversal probability.

1. Introduction

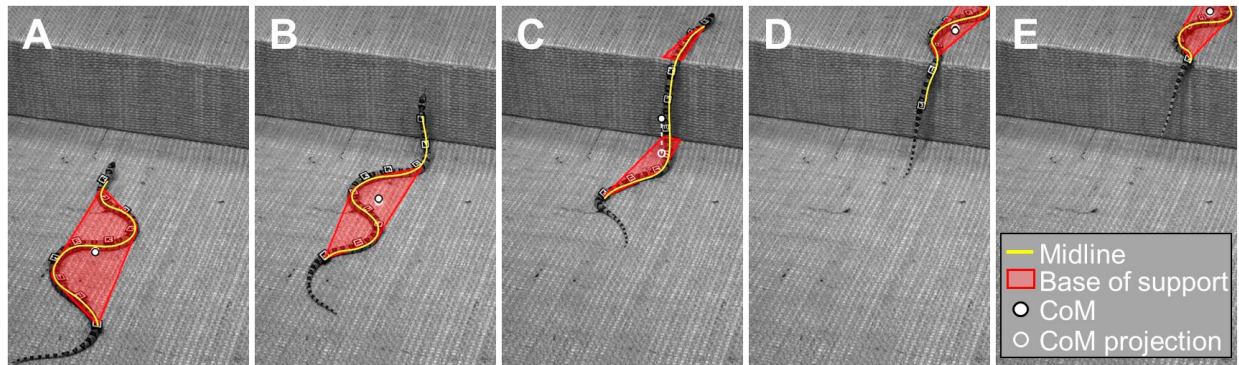


Fig. 1. A snake combines body lateral undulation and cantilevering to traverse a large step stably [1].

Representative snapshots of a kingsnake traversing a large step (oblique view) with base of support and center of mass overlaid. (A) Before cantilevering. (B) During cantilevering but before reaching upper surface. (C) After reaching upper surface. (D) Lifting off lower surface. (E) After the entire body reaches upper surface. In each snapshot, yellow curve shows body midline, red polygon shows base of support formed by body sections in contact with horizontal surfaces, white point shows center of mass, and white circle and dashed line show projection of center of mass onto a horizontal surface.

Snakes are masters of locomotion across different environments [2]. With their elongate, flexible body [3] of many degrees of freedom [4], snakes can use various planar gaits to move on flat surfaces, be it open [5–7], confined [5–7], or with small obstacles that can be circumvented [6,8]. Snakes can also deform their body out of plane to move across complex environments [1,9–12] (for a review, see [1] Supplementary Information). In these situations, out-of-plane body deformation can challenge stable locomotion [12–14], which is rarely an issue on flat surfaces with planar gaits. To maintain stability, arboreal snakes grip or brace against branches [9,11,15,16] and carefully distribute body weight [16,17]; sidewinders depress portions of the body into sand and brace against it without causing avalanche, while minimizing out-of-plane deformation [12]. However, we still know relatively little about how snakes maintain stability when surmounting obstacles such as boulders that are too large and smooth to gain such “anchor points” by gripping or bracing.

With a snake-like slender, reconfigurable body, snake robots hold the promise as versatile platforms to traverse diverse environments [18–20] for critical applications like search and rescue and building inspection [21,22]. Similar to snakes, snake robots are inherently stable when they use planar gaits on flat surfaces [23,24] but face stability challenges when they deform out of plane in more complex environments [12–14,25–27]. In branch-like terrain and confined spaces and on sandy slopes, snake robots also maintain stability by gripping or bracing against the surfaces or depressed sand [12,28–30]. Surmounting large, smooth obstacles like steps has often been achieved by using a simple, follow-the-leader gait [31–41], in which the body deforms nearly within a vertical plane with little lateral deformation and hence a narrow base of ground support. Only two previous snake robots deliberately used lateral body deformation for a wide base of support when traversing large steps [28,39,40]. Regardless, all these previous snake robots rely on careful planning and control of motion to maintain continuous static stability and thus often traverse at low speeds. Better understanding of the stability challenges of high speed locomotion over large, smooth obstacles can help snake robots traverse more rapidly and stably.

In a recent study [1], our group studied the generalist kingsnake traversing large steps by partitioning its body into sections with distinct functions (Fig. 1). The body sections below and above the step always undulate laterally on horizontal surfaces to propel the animal forward, while the body section in between cantilevers in the air in a vertical plane to bridge the height increase. An important insight was that lateral body undulation helps maintain stability by creating a wide base of ground support to resist lateral perturbations (Fig. 1, red regions). Without it, when a long body section is cantilevering in the air but has not reached the upper surface (Fig. 1B), a significant roll perturbation can tip the animal over. Thanks to body partitioning with lateral undulation, the snake traversed steps as high as 25% body length (or 30% snout-vent length) with perfect stability [1]. A signature of its perfect stability was that the laterally undulating body sections never lifted off involuntarily from horizontal surfaces before and after cantilevering.

In this study, we take the next step in understanding the stability principles of large step traversal using lateral undulation combined with cantilevering, by testing two hypotheses: (1) roll stability

diminishes as step becomes higher; and (2) body compliance improves surface contact statistically and reduces roll instability. The kingsnake did not attempt to traverse steps higher than 25% body length (on which it maintains perfect stability) and their body compliance cannot be modified without affecting locomotion. Thus, to test these two hypotheses, we developed a snake robot as a physical model which we could challenge with higher steps and whose body compliance could be modified. The second hypothesis was motivated by the observation during preliminary experiments that the robot with a rigid body often rolled to the extent of involuntary lift-off from horizontal surfaces, in contrast to the snake with compliant body [3] that never did so (see **Section 2.5** for details).

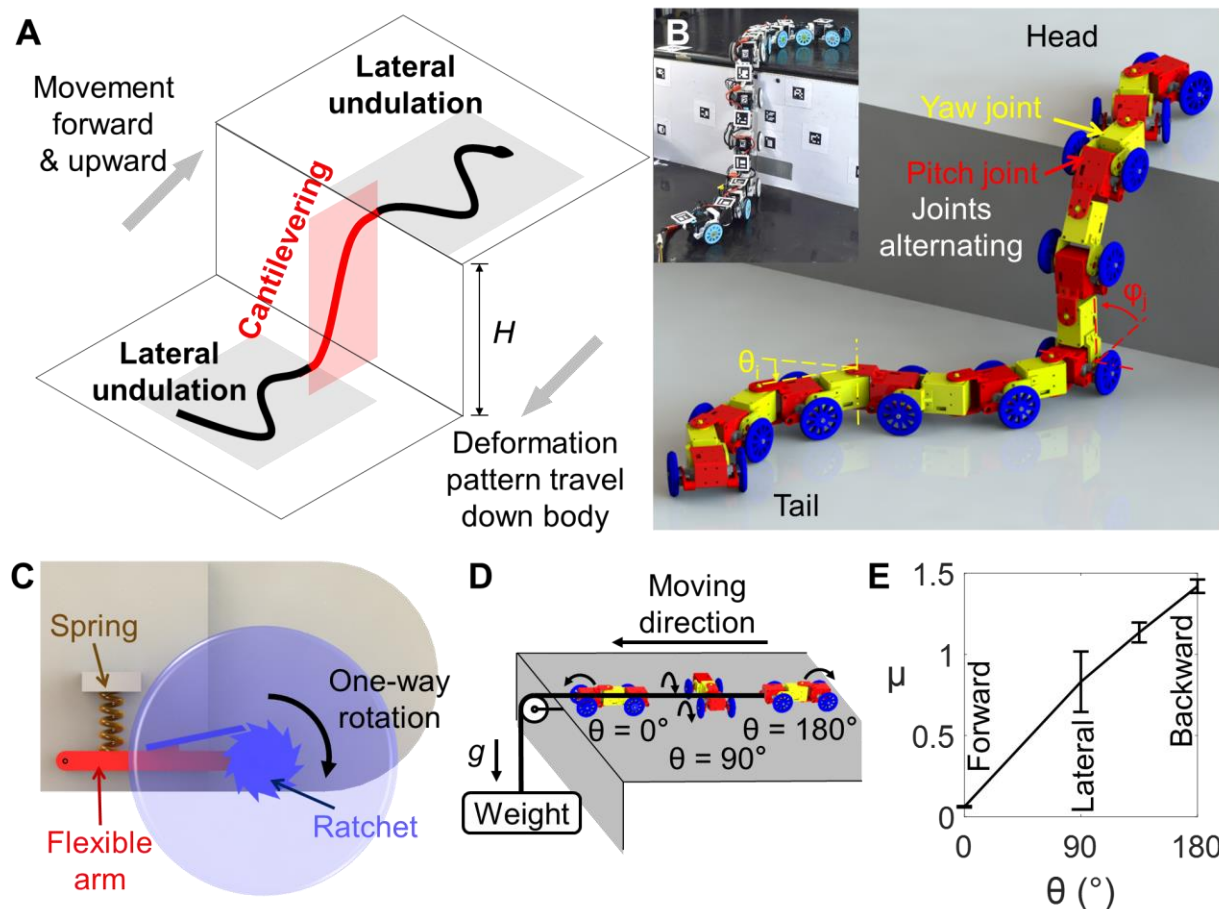


Fig. 2. Gait and mechanical design of snake robot. (A) Partitioned gait template from kingsnakes combining lateral undulation and cantilevering to traverse a large step [1]. Lateral undulation can be simply controlled and varied using a few wave parameters, such as wavelength, amplitude, and frequency. (B) The

snake robot consists of serially connected segments with alternating pitch (red) and yaw (yellow) joints and one-way wheels (blue). **(C)** Close-up view of a one-way wheel (blue) attached to each pitch segment, which only rotates forward via a ratchet mechanism. To add mechanical compliance, wheel connects to body segment via a suspension system with a spring (brown) and a flexible arm (red). Suspension is disabled in rigid robot experiments by inserting a lightweight (0.4 g) block with the same length as natural length of spring. **(D)** Experimental setup to measure kinetic friction coefficient. Three segments are dragged by a weight using a string through a pulley with various orientation angle θ between body long axis and direction of drag force. $\theta = 0^\circ$, 90° , and 180° are for sliding in body's forward, lateral, and backward directions, respectively. Arrow on one-way wheel shows its direction of free rotation. **(E)** Kinetic friction coefficient as a function of body orientation θ . Error bars show ± 1 s.d. See Movie 1 for demonstration of robot mechanisms.

2. Physical modeling with rigid snake robot

2.1. Mechanical design

Our snake robot used the partitioned gait template (Fig. 2A) from our recent animal observations [1]. The robot was 107 cm long, 8.2 cm tall, and 6.5 cm wide and weighed 2.36 kg excluding off-board controllers and extension cables. To enable large body deformation both laterally and dorsoventrally for traversing large steps (and complex 3-D terrain in general), the robot consisted of 19 segments with 19 servo motors connected by alternating pitch (red) and yaw (yellow) joints (Fig. 2B, Movie 1, see details in **Supplementary Material**), similar to [42]. We refer to segments containing pitch or yaw joint servo motors as pitch or yaw segments, respectively.

An anisotropic friction profile, with smaller forward friction than backward and lateral friction, is critical to snakes' ability to move on flat surfaces using lateral undulation [43]. To achieve this in the robot, we added to each pitch segment a pair of one-way wheels (48 mm diameter, with a rubber O-ring on each wheel) realized by a ratchet mechanism similar to [44] (Fig. 2B, C, blue, Movie 1). The one-way wheels unlocked when rotating forward and locked when rotating backward, resulting in a small forward rolling

friction and a large backward sliding friction, besides a large lateral sliding friction. We measured the kinetic friction coefficient at various body orientation (Fig. 2D, see details in **Supplementary Material**) and confirmed that forward friction was indeed smaller than backward and lateral friction (Fig. 2E).

2.2. Control of body lateral undulation and cantilevering

To generate lateral undulation on the robot's body sections below and above the step, we applied a serpenoid traveling wave spatially on the body shape with sinusoidal curvature [18] in the horizontal plane, which propagated from the head to the tail. The wave form, with a wavenumber of 1.125, was discretized onto the robot's yaw segments in these two sections, by actuating each yaw joint to follow a temporal sinusoidal wave with an amplitude of 30°, a frequency of 0.25 Hz, and a phase difference of 45° between adjacent yaw joints. The traveling wave form in the section below the step immediately followed that above, as if they formed a single wave, if the cantilevering section was not considered. We chose a serpenoid traveling wave because it is similar to that used by kingsnakes and easy to implement in snake robots [18,45,46]. We chose wave parameters from preliminary experiments and kept them constant in this study to study the effect of step height and body compliance.

To generate cantilevering on the section in between, for each step height tested, we used the minimal number of pitch segments required to bridge across the step. The cantilevering section was kept straight and as vertical as possible, except that the two most anterior pitch segments pitched forward for the anterior undulating body section to gain proper contact with the upper surface (Fig. S2A, see details in **Supplementary Material**). This shape was calculated based on the step height measured from online camera tracking before body cantilevering started and remained the same while traveling down the body. Overall, with this partitioned gait template, control of the robot's many degrees of freedom was simplified to using only a few wave parameters.

To propagate the three partitioned sections down the robot as it moved forward and upward onto the step, we used the measured positions of the robot's segments to conduct feedback logic control (Fig. S2C) similar to [40]. An online camera tracked ArUco markers attached to each pitch segment and the step

surfaces, and the distance of each segment relative to the step in the forward and upward direction was calculated. This distance was used to determine when each segment should transition from lateral undulation to cantilevering or conversely. Below we refer to this process as section division propagation. See more technical details of robot control in **Supplementary Material**.

Apart from the experimenter starting and stopping it, the robot's motion to traverse the step was automatically controlled by a computer (Fig. S2B). The experimenter stopped robot when it: (1) flipped over, (2) became stuck for over 10 undulation cycles, or (3) traversed the step.

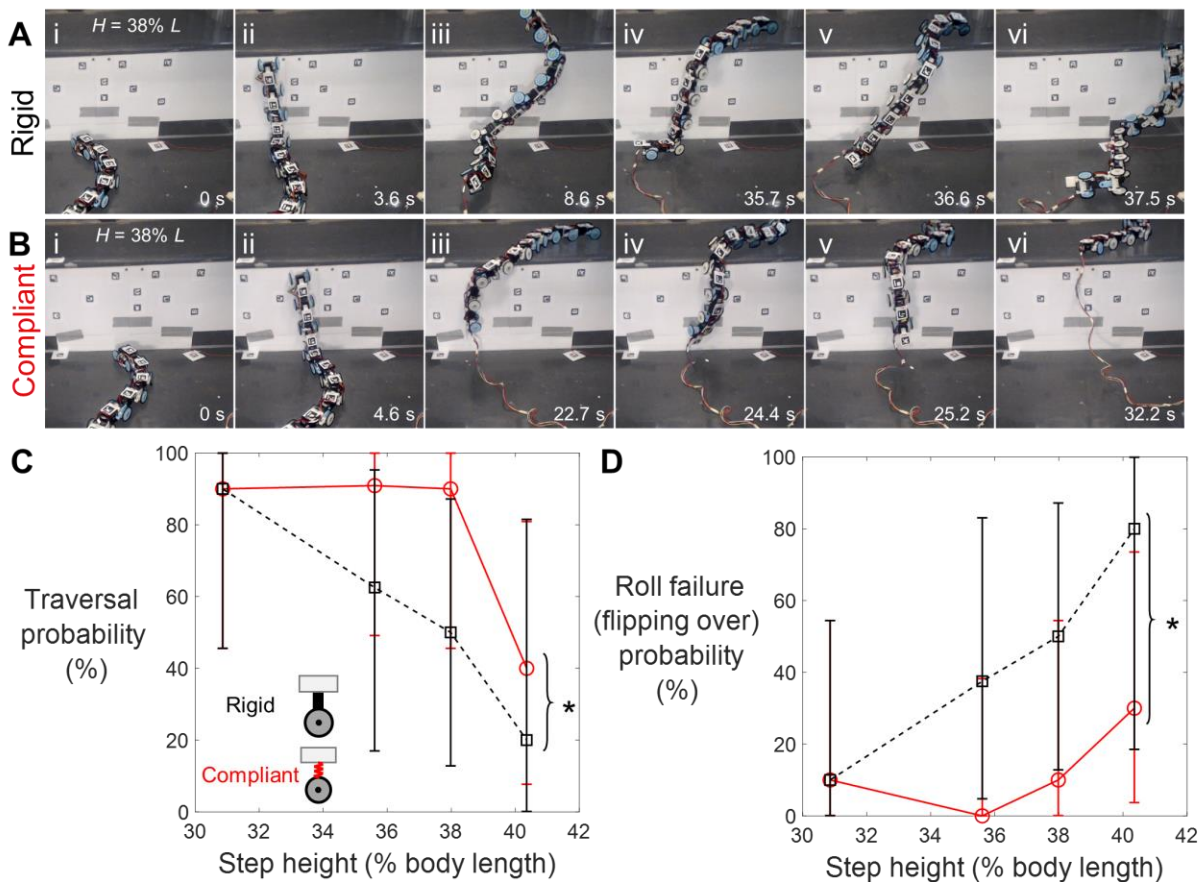


Fig. 3. Traversal performance of robot. (A, B) Representative snapshots of robot with a rigid body (A) and a compliant body (B) traversing a step as high as 38% body length. Body rolling back and forth (wobble) is visible in (A) iii-vi and (B) iii-v. Rigid body robot failed to recover from rolling and eventually flipped over; see (A) vi and Movie 3, left for a representative video. Rolling is less severe for compliant body robot, which often recovers or transitions to other events and rarely flips over; see (B) vi and Movie 3, right for a representative video. (C) Traversal probability (%) vs Step height (% body length) for Rigid and Compliant robots. (D) Roll failure (flipping over) probability (%) vs Step height (% body length) for Rigid and Compliant robots. Error bars represent standard deviation. Asterisks indicate significant differences between Rigid and Compliant robots at the 38% height level.

3, right for a representative video. **(C)** Traversal probability as a function of step height. Bracket and asterisk show a significant difference between rigid and compliant body robot ($P < 0.05$, multiple logistic regression). **(D)** Effect of body compliance on probability of roll failure (i.e., flipping over, see **Section 2.4**). Bracket and asterisk represent a significant difference between rigid and compliant body robot ($P < 0.005$, multiple logistic regression). In (C) and (D), black dashed is for rigid body robot; red solid is for compliant body robot. Error bars show 95% confidence intervals.

2.3. Traversal probability diminishes as step becomes higher

To test our first hypothesis, we challenged the robot to traverse increasingly large, high friction step obstacles (Fig. S1A), with step height $H = 33, 38, 41$, and 43 cm, or $31, 36, 38$, and 40% of robot length L (see representative trial in Fig. 3A, Movies 2, and Movie 3, left). Using body lateral undulation combined with cantilevering, the robot traversed a step as high as near a third of body length ($31\% L$) with a high probability of 90% (Fig. 3C, black dashed). In addition, its motion during traversal was more dynamic than previous snake robots that traverse steps using quasi-static motion (Movie 2 and Movie 3, left). However, as it attempted to traverse higher steps, the robot struggled (Movie 3, left) and its traversal probability quickly decreased ($P < 0.005$, simple logistic regression), diminishing to 20% when step height reached $40\% L$.

2.4. Poorer roll stability on higher steps increases failure

To determine whether the diminishing traversal probability was caused by diminishing roll stability, we recorded high speed videos of all experimental trials (Fig. S1B). Observation of these videos revealed that failure to traverse was a result of one or a sequence of adverse events (Figs. 4, 5, Movie 4).

(1) Imperfect lift timing (Fig. 4A-B; Fig. 5, gray). This includes lifting too early (Fig. 4A) or late (Fig. 4B) due to inaccurate estimation of body forward position relative to the step. Noise in the system, both mechanical (e.g., variation in robot segment and surface friction) and in feedback control (e.g., camera noise, controller delay), resulted in trial-to-trial variation of robot motion and interaction with the step, leading to inaccurate position estimation. With underestimation, a segment still far away from the step was

lifted too early (Fig. 4A, segment between i and $i+1$). With overestimation, a segment close to the step was lifted too late and pushed against the step (Fig. 4B, segment between i and $i+1$). These control imperfections often triggered other adverse events stochastically, as described below.

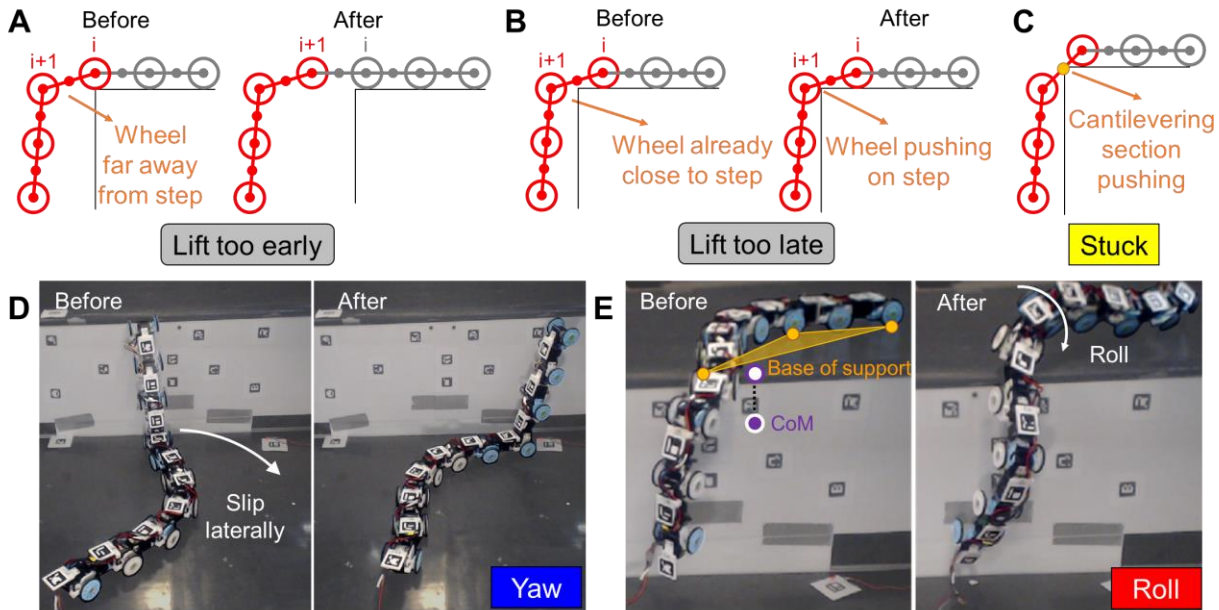


Fig. 4. Adverse events leading to failure. (A) Lift early: robot lifts up a segment too early before preceding segment moves onto the upper surface. (B) Lift late: robot lifts up a segment too late and a cantilevering segment closest to top edge of step pushes against it. In (A, B), indices above wheels are from head to tail. (C) Stuck: robot becomes stuck when cantilevering section pushes against step, with no overall direction or position change. This happens when robot belly instead of wheels contacts top edge of step. In (A-C), red and gray sections are cantilevering and undulating sections. (D) Yaw: robot yaws due to lateral slipping of body sections below and/or above step. (E) Roll: robot rolls with loss of contact below and/or above step, purple and white points are the center of mass (CoM) and its projection onto the upper horizontal surface. In (C) and (E), orange points are contact points, and orange shade is base of support. See Movie 4 for examples of (C-E).

(2) Stuck (Fig. 4C; Fig. 5, yellow). The robot was occasionally stuck when its cantilevering section pushed against the step with no substantial body yawing or rolling. After becoming stuck, the robot always eventually recovered within 10 undulation periods and succeeded in traversing (Fig. 5, no purple arrows).

(3) Yawing (Fig. 4D; Fig. 5, blue). The robot often yawed substantially when the sections below and/or above step slipped laterally. This was always triggered by imperfect lift timing (Fig. 5, arrows from gray to blue box) which led the cantilevering section to push against the vertical surface (even with lifting too early, the extra weight suspended in the air sometimes resulted in sagging of the cantilevering section, which in turn pushed against the vertical surface). The push resulted in a yawing torque too large to be overcome by the frictional force on the undulating sections from the horizontal surfaces. Because of this, yawing was often accompanied by small lift-off and slip of the undulating segments, which could lead to rolling (Fig. 5, blue arrows), described below. Yawing could also compromise segment position estimation and sometimes led to further imperfect lift timing (Fig. 5, arrows from blue to gray box).

(4) Rolling (Fig. 4E; Fig. 5, red). The robot rolled about the fore-aft axis substantially as the center of mass (Fig. 4E, purple point) projection (white point) moved out of the base of support (orange shade). Sometimes, this instability was induced by a sudden shift of center of mass position during segment lifting. At other times, this instability was induced by sudden shrinking of base of support due to loss of surface contact, which resulted from either small lift-off and/or slip of segments due to yawing or the last segment lifting off the lower surface. When rolling occurred, the robot suddenly lost many contacts from the horizontal surfaces and often lost thrust and stability. Sometimes the robot could roll back by its own bending motion (Fig. 3B iv-v). If not, it would flip over (and sometimes fell off the step) (Fig. 3A, v-vi; Movie 4), resulting in failure to traverse (Fig. 5, red arrows). Hereafter, we refer to the robot flipping over due to rolling as roll failure.

For all step heights tested, we observed a diversity of pathways stochastically transitioning among these adverse events (Fig. 5). Given the diverse, stochastic transitions, statistical trends emerged in their pathways. First, failure was always directly resulting from rolling to the extent of flipping over, i.e. roll failure (Fig. 5, red arrows). In addition, as step height increased from 31% L to 40% L , roll failure (flipping

over) became more likely, from 10% to 80% probability (Fig. 5A-D, red arrows; Fig. 3D, black dashed; $P < 0.05$, simple logistic regression), which resulted in decreasing traversal probability from 90% to 20% (Fig. 3C, black dashed). This confirmed our first hypothesis that increasing step height diminishes roll stability. This diminish was a direct result of the shorter undulating body sections for lateral support as the cantilevering body section lengthened as step height increased.

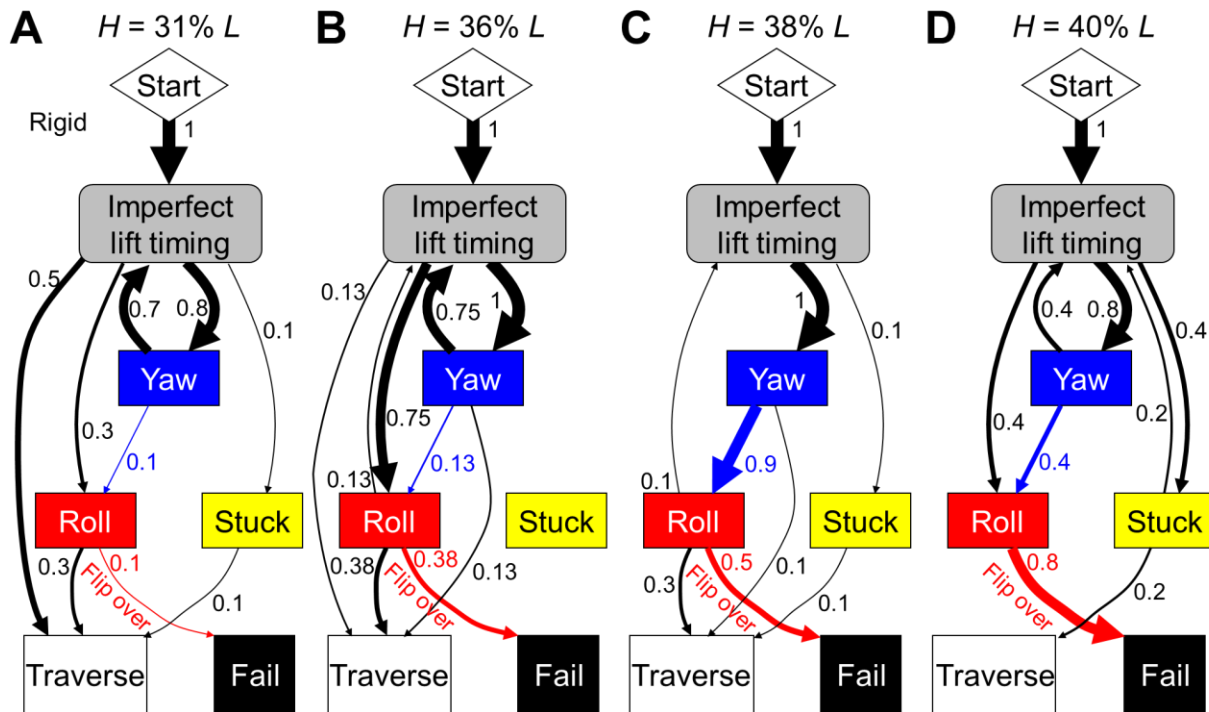


Fig. 5. Transition pathways of rigid body robot among adverse events to traverse or fail. (A) Step height $H = 31\% L$. (B) $H = 36\% L$. (C) $H = 38\% L$. (D) $H = 40\% L$. Each arrow is a transition between nodes, with arrow thickness proportional to its probability of occurrence, shown by number next to it. Probability of occurrence here is the ratio of the number of trials in which a transition occurs to the total number of trials; it is different from transition probability in Markov chains. If a transition occurs multiple times in a trial, it is only counted once.

2.5. Comparison with snakes

Comparison of robot with animal observations [1] revealed and elucidated the snake's better ability to maintain stability over the robot. First, the robot always suffered imperfect body lift timing (Fig. 5, arrows from start to gray box), which was rarely observed in the snake [1]. Second, the robot's laterally undulating body sections often suffered large yawing ($\geq 80\%$ probability, Fig. 5, blue) and rolling ($\geq 40\%$, Fig. 5, red). In contrast, the snake's undulating body sections rarely rolled on the horizontal surfaces, even when step friction was low and the animal slipped substantially [1]. Third, when step friction was high, the robot sometimes became stuck (Fig. 5, yellow), whereas the snake always smoothly traversed [1]. These indicate that the snake is better at accommodating noise and perturbations in control, design, and the environment (e.g., improper timing, unexpected forces and slippage, variation in step surface height and friction) to maintain effective body-terrain interaction.

Besides the animal's better ability to use sensory feedback to control movement in complex environments [47], two morphological features of the snake body likely contributed to its better ability to maintain stability—being more continuous (over 200 vertebrae [4] vs. the robot's 19 segments) and more compliant [3]. The latter is particularly plausible considering that the introduction of mechanical compliance to end effectors has proven crucial in robotic tasks where contact with the environment is essential, e.g., grasping [48–50], polishing [51], and climbing [52,53] robots (for a review, see [54]). Although many snake robots have used compliance in control to adapt overall body shape to obstacles [55–58], the use of mechanical compliance to better conform to surfaces locally was less considered [56,59], especially for improving stability. These considerations inspired us to test our second hypothesis that body compliance improves surface contact statistically and reduces roll instability.

3. Physical modeling with compliant snake robot

3.1. Suspension to add mechanical compliance

To test our second hypothesis, we added mechanical compliance to the robot by inserting between each one-way wheel and its body segment a suspension system inspired by [59] (Fig. 2C). The suspension of each wheel (even the left and right on the same segment) could passively compress independently to

conform to surface variation (by up to 10 mm displacement of each wheel). From our second hypothesis that body compliance improves surface contact statistically and reduces roll instability, we predicted that this passive conformation would increase traversal probability and reduce roll failure (flipping over) probability, especially for larger steps. The suspension system was present but disengaged in the rigid robot experiments for direct comparison.

3.2. Body compliance increases traversal probability

The compliant body robot maintained high traversal probability over a larger range of step height than the rigid robot, consistently succeeding 90% of the time as step height increased from 31% L to 38% L (Fig. 3C, red solid). Like the rigid body robot, the compliant body robot's motion during traversal was also more dynamic than previous robots using quasi-static gaits (Movie 3, right). Traversal probability only decreased for step height beyond 38% L ($P < 0.05$, pairwise Chi-square test). For the large step heights tested, adding body compliance increased traversal probability ($P < 0.05$, multiple logistic regression). These observations were in accord with our prediction from the second hypothesis.

3.3. Body compliance reduces roll failure probability

To test our second hypothesis, specifically that body compliance reduces roll instability, we compared the compliant body robot's transition pathways among adverse events (Fig. 6) to those of the rigid body robot (Fig. 5). The compliant body robot still stochastically transitioned among adverse events. However, two improvements were observed in the statistical trends of the transition pathways.

First, the compliant body robot suffered roll failure (flipping over) less frequently (Fig. 5 vs. Fig. 6, red arrows; Fig. 3D; $P < 0.005$, multiple logistic regression), especially after yawing occurred (Fig. 5 vs. Fig. 6, blue arrows). It also experienced less frequent back and forth rolling (wobbling) (Fig. 3B; Movie 3, right) than the rigid body robot (Fig. 3A; Movie 3, left). This confirmed our hypothesis that body compliance reduces roll instability. However, body compliance did not eliminate rolling, and the compliant robot still slipped frequently. These observations were in accord with our prediction from the second hypothesis.

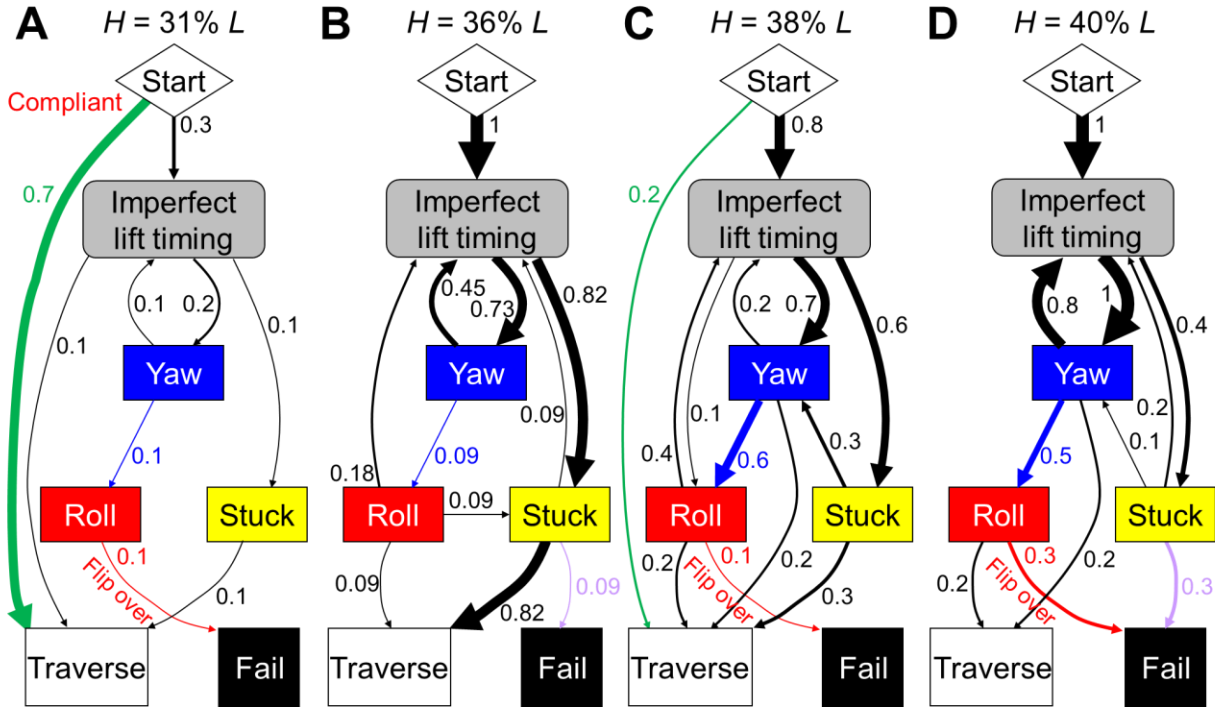


Fig. 6. Transition pathways of compliant body robot among adverse events to traverse or fail. (A) Step height $H = 31\% L$. (B) $H = 36\% L$. (C) $H = 38\% L$. (D) $H = 40\% L$. See Fig. 5 for definition of transition diagrams.

Second, the compliant body robot suffered imperfect lift timing less frequently than the rigid body robot (Fig. 5 vs. Fig. 6, green arrows), which eventually resulted in more frequent traversal for all step heights above 31% L (Fig. 5 vs. Fig. 6, sum of all black arrows into white box). This was because, even when lifting was too early or too late, the compliant body robot could often afford to push against the vertical surface without triggering catastrophic failure from yawing or rolling before section division propagation resumed.

However, the compliant body robot became stuck more frequently (Fig. 5 vs. Fig. 6, arrow from gray to yellow box) and failed more frequently as a result (Fig. 5 vs. Fig. 6, purple arrow). This was because compression of the suspension lowered ground clearance of the segments. This stuck failure mode was

always directly triggered by lifting too early. This is a limitation of the robot's discrete, few degree-of-freedom body.

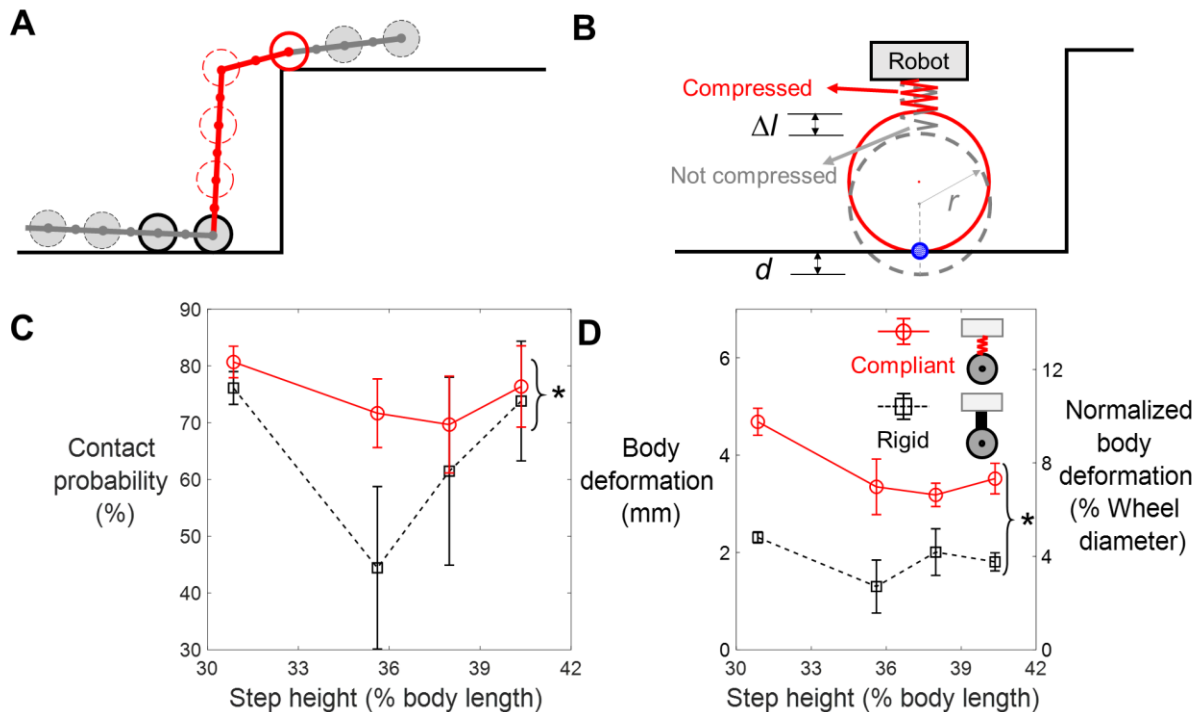


Fig. 7. Effect of body compliance on contact probability and body deformation. **(A)** Example side view schematic to define contact probability. Gray are laterally undulating body sections and red is cantilevering body section. In this example, three wheels of undulating section are in contact with surface (solid) and four are not (dashed), and contact probability = $3/(3 + 4) = 43\%$. **(B)** Definition of body deformation. Red solid schematic shows actual wheel position with suspension compressed, and gray dashed one shows wheel position assuming no suspension compression. Blue circle shows point of contact between wheel and surface. Body deformation Δl is approximated by virtual wheel penetration d into surface. **(C)** Contact probability as a function of step height. **(D)** Body deformation as a function of step height. In (C) and (D), black dashed is for rigid body robot; red solid is for compliant body robot. Error bars show ± 1 s.d. Brackets and asterisks represent a significant difference between rigid and compliant body robot ($P < 0.001$, ANCOVA).

3.4. Body compliance improves contact statistically

To further test our second hypothesis, specifically that body compliance improves surface contact statistically, we compared contact probability between the rigid and compliant body robot. Contact probability was defined as the ratio of the number of wheels contacting horizontal surfaces in the laterally undulating body sections to the total number of wheels in these two sections (Fig. 7A). In addition, we calculated body deformation as how much each wheel suspension was compressed for these two sections (Fig. 7B). Both wheel contact and body deformation were determined by examining whether any part of each wheel penetrated the step surface assuming no suspension compression, based on 3-D reconstruction of the robot from high speed videos. Both were averaged spatiotemporally over the traversal process across all pitch segments in these two sections combined for each trial. See details in **Supplementary Material**.

For all step heights tested, the compliant body robot had a higher contact probability than the rigid body robot (Fig. 7C; $P < 0.001$, ANCOVA). This improvement was a direct result of larger body deformation (Fig. 7D; $P < 0.0001$, ANCOVA): the rigid body robot only deformed around 2 mm or 4% wheel diameter (which occurred in the rubber on both the wheels and step surfaces); by contrast, the compliant robot's suspension deformed around 4 mm or 8% wheel diameter, a 100% increase.

3.5. Body compliance reduces severity of body rolling

Body rolling would result in lateral asymmetry in how the robot conforms with the surface between the left and right sides of the body. Thus, to quantify the severity of body rolling, we calculated the difference (absolute value) in surface conformation between left and right wheels (Fig. 8) excluding the cantilevering section. Surface conformation was defined as the virtual penetration of a wheel in contact (positive distance) or the minimal distance from the surface of a wheel lifted off (negative distance) (Fig. 8A inset, right or left wheel). A larger difference (absolute value) in surface conformation between left and right sides means more severe rolling. Surface conformation difference was averaged spatiotemporally over the traversal process across all pitch segments separately for the body sections below and above the step for each trial. See details in **Supplementary Material**.

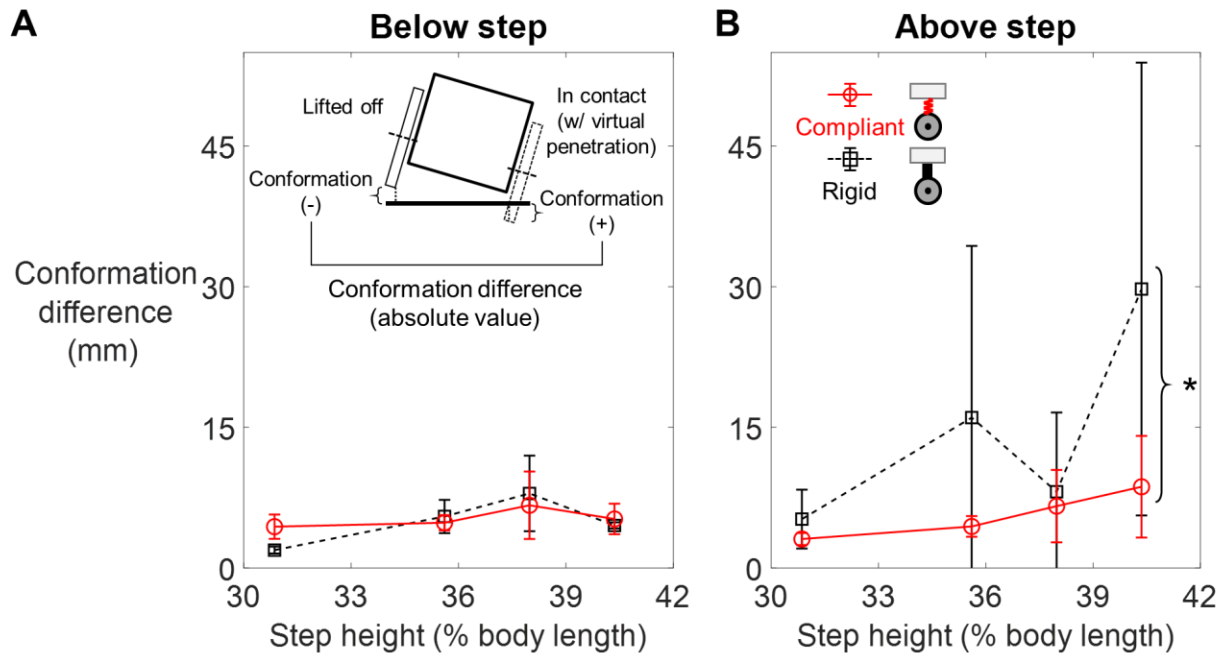


Fig. 8. Effect of body compliance on surface conformation difference. (A, B) Surface conformation difference between left and right wheels as a function of step height for body sections below (A) and above (B) step. Black dashed is for rigid body robot; red solid is for compliant body robot. Error bars show ± 1 s.d. Brackets and asterisks represent a significant difference between rigid and compliant body robot ($P < 0.005$, ANCOVA). Inset in (A) shows front view schematic to define surface conformation difference (see text for detail).

For all step heights tested, body compliance reduced lateral asymmetry in surface conformation for the body section above the step (Fig. 8B; $P < 0.005$, ANCOVA), although not for the section below (Fig. 8A; $P > 0.05$, ANCOVA). This means that the compliant body robot had less severe body rolling above the step (Fig. 3B; Movie 3, right) and was more stable during traversal. Such better surface conformation likely allowed the compliant body robot to generate ground reaction forces more evenly along the body [60] to better propel itself forward and upward, which the rigid robot with poorer surface conformation struggled to do. The compliant body robot still wobbled and slipped more substantially than the snakes [1].

All these observations from the compliant body robot confirmed our second hypothesis that body compliance improves surface contact statistically and reduces roll instability.

3.6. Body compliance increases energetic cost

Not surprisingly, these benefits came with a price. The electrical power consumed by the robot increased when body compliance was added (Fig. S3; $P < 0.0001$, ANCOVA; see details in **Supplementary Material**). We speculate that this was due to an increase in energy dissipation from larger friction dissipation against the surfaces due to higher contact probability, viscoelastic response [54] of the suspension, and more motor stalling and wheel sliding due to more frequently getting stuck. Electrical power consumption decreased with step height (Fig. S3; $P < 0.0001$, ANCOVA), which may result from the decrease in the number of laterally undulating segments that dissipated energy during sliding against the surfaces. We noted that the electrical energy consumed (power integrated over time) during traversal was two orders of magnitude larger than the mechanical work needed to lift the robot onto the step; the majority of the energy was not used to do useful work [61].

4. Contribution to robotics

Our study advanced the performance of snake robots traversing large steps. When normalized to body length, our robot (both rigid and compliant body, Fig. 9, red and black) achieved step traversal speed higher than most previous snake robots (gray) and approaching that of kingsnakes (blue). In addition, our compliant robot maintained high traversal probability (90%) even when the step was as high as 38% body length (Fig. 3C, red solid), without loss of traversal speed compared to the rigid body robot ($P > 0.05$, pairwise two-sample t -test). These improvements were attributed to the inherent roll stability from body lateral undulation and an improved ability to maintain surface contact via body compliance, which alleviated the need for precise control for static stability and enabled dynamic traversal. The only other snake robot that achieved comparable step traversal speed (T² Snake-3 [36]) used active wheels to drive the body while only deforming in a vertical plane and thus had low roll stability. It also pushed against and propelled its wheels up the vertical surface, which reduced the load of pitching segments and increased the

maximal cantilevering length. We note that our robot still has the potential to achieve even higher speeds with high traversal probability, because in our experiments the motors were actuated at only 50% full speed to protect the robot from breaking after drastically flipping over as well as motor overload due to inertial forces and we have yet to systematically test and identify optimal serpenoid wave parameters [62].

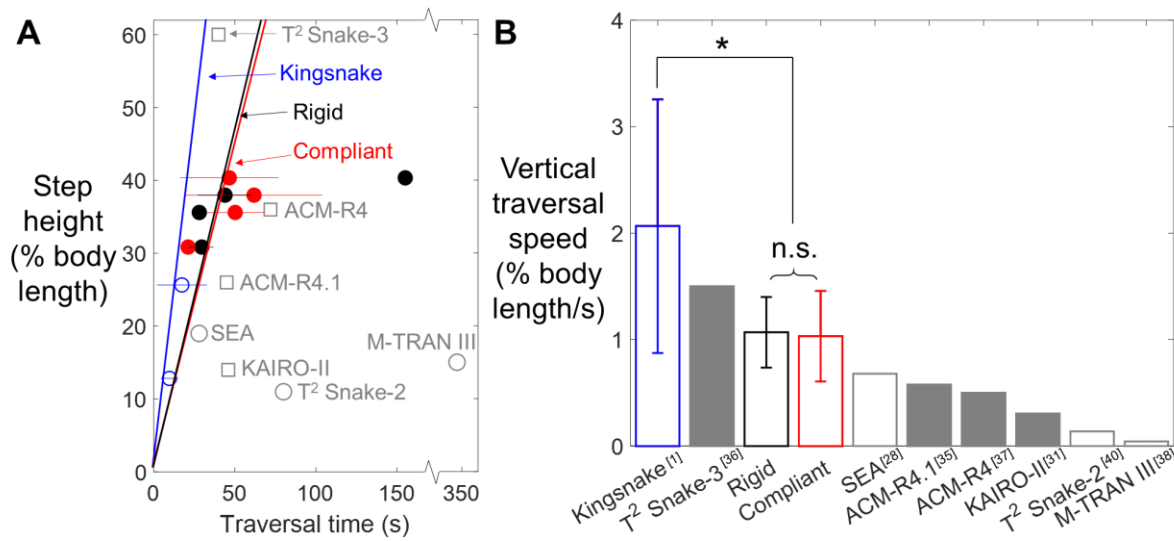


Fig. 9. Comparison of traversal performance of our robot with previous snake robots and the kingsnake. **(A)** Maximal traversable step height (normalized to body length) as a function of traversal time for kingsnake (blue), our robot with rigid (black) and (red) compliant body, and previous snake robots with data available (gray squares: with active propellers; gray circles: no active propellers). Several previous robots with no traversal time reported are not included [21,33,34,42,63,64]. **(B)** Vertical traversal speed normalized to body length. Vertical traversal speed, i.e., normalized step height divided by traversal time, is the slope of lines connecting each data point to the origin in (A). Thus, a higher slope indicates a larger vertical traversal speed. Speeds of previous robots are the fastest reported values (vs. average in ours) from [28,31,35–38,40] or accompanying videos. See **Supplementary Material** for details of speed calculation. Bracket and asterisk represent a significant difference in vertical traversal speed ($P < 0.005$, pairwise two-sample t -test). n.s. represents no significant difference ($P > 0.05$, pairwise two-sample t -test). In (A, B), error bars show ± 1 s.d.

5. Summary and future work

Inspired by our recent observations in snakes, we developed a snake robot as a physical model and performed systematic experiments to study stability principles of large step traversal using a partitioned gait that combines lateral body undulation and cantilevering. Our experiments confirmed two hypotheses: (1) roll stability diminishes as step becomes higher; and (2) body compliance improves surface contact statistically and reduces roll instability. In addition, thanks to the integration of lateral body undulation to resist roll instability with anisotropic friction for thrust, our snake robot traversed large step obstacles more dynamically than previous robots with higher traversal speeds (normalized to body length), approaching animal performance. Moreover, by further adding body compliance to improve surface contact, our snake robot better maintained high traversal probability on high steps without loss in traversal speed. Although our discoveries were made on a simple large step with only vertical body compliance, the use of body lateral undulation and compliance to achieve a large base of support with reliable contact for roll stability is broadly useful for snakes and snake robots traversing other large, smooth obstacles in terrain like non-parallel steps [36,39], stairs [28,32,36], boulders, and rubble [22,56].

Given these advances, the snake's locomotion over large obstacles is still superior, without any visible wobble or slip on high friction steps [1]. This is likely attributed to the animal's more continuous body, additional body compliance in other directions (e.g., rolling, lateral), and ability to actively adjust its body [65] using sensory feedback [66] to conform to the terrain beyond achievable by passive body compliance. Future studies should elucidate how snakes, and how snake robot should, use tactile sensory feedback control [56–58,60] and combine control compliance [35,58] with mechanical compliance [54,60,67] along multiple directions [52] to stably traverse large, smooth obstacles.

Finally, as our study begins to demonstrate, locomotion in 3-D terrain with many large obstacles often involves stochastic transitions, which are statistically affected by locomotor-terrain physical interaction [68–71] (e.g., step height and body compliance here). A new statistical physics view of locomotor transitions [72] will help accelerate the understanding of how animals use or mitigate such

statistical dependence and its application in robotic obstacle traversal using physical interaction in the stochastic world.

Data accessibility

This paper has Supplementary Material, including:

Materials and Methods

Fig. S1. Experimental setup and 3-D kinematics reconstruction.

Fig. S2. Controller design.

Fig. S3. Effect of body compliance on electrical power.

Table S1. Sample size.

Movie 1. [Snake robot uses a snake-like partitioned gait to traverse a large step rapidly.](#)

Movie 2. [Flipping over of a snake robot when traversing a large step.](#)

Movie 3. [Adding body compliance to a snake robot.](#)

Movie 4. [Comparison of large step traversal between rigid and compliant body snake robot.](#)

Excel form S1. Data reported in the paper.

Authors' contributions

QF designed study, developed robot, performed experiments, analyzed data, and wrote the paper;

CL designed and oversaw study and revised the paper. Both authors gave final approval for publication.

Competing interest

The authors declare no competing interests.

Funding

This work was supported by a Burroughs Wellcome Fund Career Award at the Scientific Interface, an Arnold & Mabel Beckman Foundation Beckman Young Investigator award, and The Johns Hopkins University Whiting School of Engineering start-up funds to CL.

Acknowledgements

We thank Hongtao Wu and Zhiyi Ren for building the frame for multi-camera setup; Tommy Mitchel and Sean Gart for advice on animal data analysis; Nansong Yi and Huidong Gao for help with robot design; Zhiyi Ren for providing initial codes of robot control; and Ratan Othayoth, Qihan Xuan, Yuanfeng Han, Yulong Wang, and Henry Astley for discussion.

References

1. Gart SW, Mitchel TW, Li C. 2019 Snakes partition their body to traverse large steps stably. *J. Exp. Biol.* **59**, jeb--185991. (doi:10.1242/jeb.185991)
2. Houssaye A, Boistel R, Böhme W, Herrel A. 2013 Jack-of-all-trades master of all? Snake vertebrae have a generalist inner organization. *Naturwissenschaften* **100**, 997–1006. (doi:10.1007/s00114-013-1102-x)
3. Penning DA, Moon BR. 2017 The king of snakes: performance and morphology of intraguild predators (*Lampropeltis*) and their prey (*Pantherophis*). *J. Exp. Biol.* **220**, 1154–1161. (doi:10.1242/jeb.147082)
4. Voris HK. 1975 Dermal scale-vertebra relationships in sea snakes (Hydrophiidae). *Copeia* , 746–757.
5. Gray J. 1946 The Mechanism of Locomotion in Snakes. *J. Exp. Biol.* **23**, 101–120.
6. Jayne BC. 1986 Kinematics of Terrestrial Snake Locomotion. *Copeia* **1986**, 915–927. (doi:10.2307/1445288)
7. Marvi H, Hu DL. 2012 Friction enhancement in concertina locomotion of snakes. *J. R. Soc. Interface* **9**, 3067–3080. (doi:10.1098/rsif.2012.0132)

8. Gray J, Lissmann HW. 1950 The kinetics of the locomotion of the grass-snake. *J. Exp. Biol.* **26**, 354–367.
9. Jayne BC, Riley MA. 2007 Scaling of the axial morphology and gap-bridging ability of the brown tree snake, *Boiga irregularis*. *J. Exp. Biol.* **210**, 1148–1160. (doi:10.1242/jeb.002493)
10. Byrnes G, Jayne BC. 2014 Gripping during climbing of arboreal snakes may be safe but not economical. *Biol. Lett.* **10**. (doi:10.1098/rsbl.2014.0434)
11. Astley HC, Jayne BC. 2009 Arboreal habitat structure affects the performance and modes of locomotion of corn snakes (*Elaphe guttata*). *J. Exp. Zool. Part A Ecol. Genet. Physiol.* **311**, 207–216. (doi:10.1002/jez.521)
12. Marvi H *et al.* 2014 Sidewinding with minimal slip: Snake and robot ascent of sandy slopes. *Science (80-.).* **346**, 224–229. (doi:10.1126/science.1255718)
13. Hatton RL, Choset H. 2010 Sidewinding on slopes. In *2010 IEEE International Conference on Robotics and Automation*, pp. 691–696. (doi:10.1109/ROBOT.2010.5509875)
14. Gong C, Hatton RL, Choset H. 2012 Conical sidewinding. *Proc. - IEEE Int. Conf. Robot. Autom.* , 4222–4227. (doi:10.1109/ICRA.2012.6225377)
15. Lillywhite HB, Lafrentz JR, Lin YC, Tu MC. 2000 The Cantilever Abilities of Snakes. *J. Herpetol.* **34**, 523–528.
16. Jayne BC, Byrnes G. 2015 The effects of slope and branch structure on the locomotion of a specialized arboreal colubrid snake (*Boiga irregularis*). *J. Exp. Zool. Part A Ecol. Genet. Physiol.* **323**, 309–321. (doi:10.1002/jez.1920)
17. Jayne BC, Herrmann MP. 2011 Perch size and structure have species-dependent effects on the arboreal locomotion of rat snakes and boa constrictors. *J. Exp. Biol.* **214**, 2189–2201. (doi:10.1242/jeb.055293)
18. Hirose S. 1993 *Biologically inspired robots: snake-like locomotors and manipulators*. Oxford University Press.
19. Walker ID, Choset H, Chirikjian GS. 2016 Snake-like and continuum robots. In *Springer*

Handbook of Robotics, pp. 481–498.

20. Nie C, Pacheco Corcho X, Spenko M. 2013 Robots on the move: Versatility and complexity in mobile robot locomotion. *IEEE Robot. Autom. Mag.* **20**, 72–82.
(doi:10.1109/MRA.2013.2248310)
21. Osuka K, Kitajima H. 2003 Development of mobile inspection robot for rescue activities: MOIRA. *Proc. 2003 IEEE/RSJ Int. Conf. Intell. Robot. Syst. (IROS 2003) (Cat. No.03CH37453)* **3**, 3373–3377. (doi:10.1109/IROS.2003.1249677)
22. Whitman J, Zevallos N, Travers M, Choset H. 2018 Snake Robot Urban Search after the 2017 Mexico City Earthquake. *2018 IEEE Int. Symp. Safety, Secur. Rescue Robot. SSRR 2018* , 1–6.
(doi:10.1109/SSRR.2018.8468633)
23. Dowling K. 1997 Limbless Locomotion : Learning to Crawl with a Snake Robot. *Most* , 1–150.
24. Hirose S, Mori M. 2004 Biologically Inspired Snake-like Robots. In *2004 IEEE International Conference on Robotics and Biomimetics*, pp. 1–7. Shenyang, China: IEEE.
(doi:10.1109/ROBIO.2004.1521742)
25. Yim M, Homans S, Roufas K. 2001 Climbing with snake-like robots. In *IFAC workshop on mobile robot technology*, pp. 21–22. (doi:10.1016/S1474-6670(17)34265-9)
26. Cappo EA, Choset H. 2014 Planning end effector trajectories for a serially linked, floating-base robot with changing support polygon. In *2014 American Control Conference*, pp. 4038–4043.
(doi:10.1109/ACC.2014.6859430)
27. Toyoshima S, Matsuno F. 2012 A study on sinus-lifting motion of a snake robot with energetic efficiency. In *2012 IEEE International Conference on Robotics and Automation*, pp. 2673–2678. IEEE. (doi:10.1109/ICRA.2012.6224829)
28. Lipkin K, Brown I, Peck A, Choset H, Rembisz J, Gianfortoni P, Naaktgeboren A. 2007 Differentiable and piecewise differentiable gaits for snake robots. *IEEE Int. Conf. Intell. Robot. Syst.* , 1864–1869. (doi:10.1109/IROS.2007.4399638)
29. Melo K, Paez L. 2012 Modular snake robot gaits on horizontal pipes. In *2012 IEEE/RSJ*

international conference on intelligent robots and systems, pp. 3099–3104.

30. Takemori T, Tanaka M, Matsuno F. 2018 Ladder Climbing with a Snake Robot. *IEEE Int. Conf. Intell. Robot. Syst.*, 8140–8145. (doi:10.1109/IROS.2018.8594411)
31. Birkenhofer C. 2010 *Adaptive Steuerung eines mehrsegmentigen Inspektionsroboters*. KIT Scientific Publishing.
32. Komura H, Yamada H, Hirose S. 2015 Development of snake-like robot ACM-R8 with large and mono-tread wheel. *Adv. Robot.* **29**, 1081–1094.
33. Takayama T, Hirose S. 2000 Development of Souryu-I connected crawler vehicle for inspection of narrow and winding space. *IECON Proc. (Industrial Electron. Conf.)* **1**, 143–148. (doi:10.1109/IECON.2000.973140)
34. Scholl K-U, Kepplin V, Berns K, Dillmann R. 2000 Controlling a multi-joint robot for autonomous sewer inspection. In *Proceedings 2000 ICRA. Millennium Conference. IEEE International Conference on Robotics and Automation. Symposia Proceedings (Cat. No. 00CH37065)*, pp. 1701–1706.
35. Takaoka S, Yamada H, Hirose S. 2011 Snake-like active wheel robot ACM-R4.1 with joint torque sensor and limiter. In *2011 IEEE/RSJ International Conference on Intelligent Robots and Systems*, pp. 1081–1086. (doi:10.1109/IROS.2011.6048084)
36. Tanaka M, Nakajima M, Suzuki Y, Tanaka K. 2018 Development and Control of Articulated Mobile Robot for Climbing Steep Stairs. *IEEE/ASME Trans. Mechatronics* **23**, 531–541. (doi:10.1109/TMECH.2018.2792013)
37. Yamada H, Hirose S. 2006 Development of Practical 3-Dimensional Active Cord Mechanism ACM-R4. *J. Robot. Mechatronics* **18**, 305–311.
38. Kurokawa H, Tomita K, Kamimura A, Kokaji S, Hasuo T, Murata S. 2008 Distributed self-reconfiguration of M-TRAN III modular robotic system. *Int. J. Rob. Res.* **27**, 373–386. (doi:10.1177/0278364907085560)
39. Nakajima M, Tanaka M, Tanaka K, Matsuno F. 2018 Motion control of a snake robot moving

between two non-parallel planes. *Adv. Robot.* **32**, 559–573.
(doi:10.1080/01691864.2018.1458653)

40. Tanaka M, Tanaka K. 2013 Climbing and descending control of a snake robot on step environments based on kinematics. *IEEE Int. Conf. Intell. Robot. Syst.* , 3285–3290.
(doi:10.1109/IROS.2013.6696823)

41. Jing G, Tosun T, Yim M, Kress-Gazit H. 2017 An End-to-End System for Accomplishing Tasks with Modular Robots : Perspectives for the AI Community. In *IJCAI*, pp. 4879–4883. Melbourne, Australia: AAAI Press.

42. Kouno K, Yamada H, Hirose S. 2013 Development of active-joint active-wheel high traversability snake-like robot ACM-R4.2. *J. Robot. Mechatronics* **25**, 559–566.

43. Hu DL, Nirody J, Scott T, Shelley MJ. 2009 The mechanics of slithering locomotion. *Proc. Natl. Acad. Sci.* **106**, 10081–10085. (doi:10.1073/pnas.0812533106)

44. Chirikjian GS, Burdick JW. 1995 The kinematics of hyper-redundant robot locomotion. *IEEE Trans Robot. Autom.* **11**, 781–793.

45. Transeth AA, Liljeback P, Pettersen KY. 2007 Snake robot obstacle aided locomotion: An experimental validation of a non-smooth modeling approach. *IEEE Int. Conf. Intell. Robot. Syst.* , 2582–2589. (doi:10.1109/IROS.2007.4399175)

46. Tanaka M, Tanaka K. 2015 Control of a Snake Robot for Ascending and Descending Steps. *IEEE Trans. Robot.* **31**, 511–520. (doi:10.1109/TRO.2015.2400655)

47. Dickinson MH, Farley CT, Full RJ, Koehl M a R, Kram R, Lehman S. 2000 How animals move: An integrative view [Review]. *Science (80-)* **288**, 100–106. (doi:10.1126/science.288.5463.100)

48. Shimoga KB, Goldenberg AA. 1996 Soft robotic fingertips: Part I: A comparison of construction materials. *Int. J. Rob. Res.* **15**, 320–334.

49. Mason MT, Rodriguez A, Srinivasa SS, Vazquez AS. 2012 Autonomous manipulation with a general-purpose simple hand. *Int. J. Rob. Res.* **31**, 688–703.

50. Truby RL, Katschmann RK, Lewis JA, Rus D. 2019 Soft Robotic Fingers with Embedded

Ionogel Sensors and Discrete Actuation Modes for Somatosensitive Manipulation. In *2019 2nd IEEE International Conference on Soft Robotics (RoboSoft)*, pp. 322–329.

51. Furukawa T, Rye DC, Dissanayake M, Barratt AJ. 1996 Automated polishing of an unknown three-dimensional surface. *Robot. Comput. Integr. Manuf.* **12**, 261–270.
52. Ruotolo W, Roig FS, Cutkosky M. 2019 Load-Sharing in Soft and Spiny Paws for a Large Climbing Robot. *IEEE Robot. Autom. Lett.* **4**, 1–1. (doi:10.1109/Lra.2019.2897002)
53. Asbeck AT. 2010 Compliant Directional Suspension for Climbing with Spines and Adhesives. Stanford University.
54. Hawkes EW, Cutkosky MR. 2018 Design of Materials and Mechanisms for Responsive Robots. *Annu. Rev. Control. Robot. Auton. Syst.* **1**, 359–384. (doi:10.1146/annurev-control-060117-104903)
55. Gong C, Tesch M, Rollinson D, Choset H. 2014 Snakes on an inclined plane: Learning an adaptive sidewinding motion for changing slopes. *IEEE Int. Conf. Intell. Robot. Syst.* , 1114–1119. (doi:10.1109/IROS.2014.6942697)
56. Takemori T, Tanaka M, Matsuno F. 2018 Gait design for a snake robot by connecting curve segments and experimental demonstration. *IEEE Trans. Robot.* **34**, 1384–1391. (doi:10.1109/TRO.2018.2830346)
57. Travers M, Whitman J, Choset H. 2018 Shape-based coordination in locomotion control. *Int. J. Rob. Res.* , 027836491876156. (doi:10.1177/0278364918761569)
58. Kano T, Ishiguro A. 2013 Obstacles are beneficial to me! Scaffold-based locomotion of a snake-like robot using decentralized control. In *IEEE International Conference on Intelligent Robots and Systems*, pp. 3273–3278. IEEE. (doi:10.1109/IROS.2013.6696821)
59. Togawa K, Mori M, Hirose S. 2000 Study on three-dimensional active cord mechanism: development of ACM-R2. *Proceedings. IEEE/RSJ Int. Conf. Intell. Robot. Syst. (IROS 2000) (Cat. No.00CH37113)*. **3**, 2242–2247. (doi:10.1109/IROS.2000.895302)
60. Kim S, Spenko M, Trujillo S, Heyneman B, Mattoli V, Cutkosky MR. 2007 Whole body

adhesion: Hierarchical, directional and distributed control of adhesive forces for a climbing robot. *Proc. - IEEE Int. Conf. Robot. Autom.* , 1268–1273. (doi:10.1109/ROBOT.2007.363159)

61. Kashiri N *et al.* 2018 An overview on principles for energy efficient robot locomotion. *Front. Robot. AI* **5**, 129. (doi:10.3389/frobt.2018.00129)

62. Saito M, Fukaya M, Iwasaki T. 2002 Serpentine locomotion with robotic snakes. *IEEE Control Syst. Mag.* **22**, 64–81. (doi:10.1109/37.980248)

63. Borenstein J, Hansen M. 2007 OmniTread OT-4 serpentine robot: new features and experiments. In *Unmanned Systems Technology IX* (eds GR Gerhart, DW Gage, CM Shoemaker), p. 656113. Orlando, Florida, USA: The international society for optics and photonics. (doi:10.1117/12.717754)

64. Suzuki K, Nakano A, Endo G, Hirose S. 2012 Development of multi-wheeled snake-like rescue robots with active elastic trunk. *IEEE Int. Conf. Intell. Robot. Syst.* , 4602–4607. (doi:10.1109/IROS.2012.6385757)

65. Jayne BC. 1988 Muscular mechanisms of snake locomotion: an electromyographic study of lateral undulation of the Florida banded water snake (*Nerodia fasciata*) and the yellow rat snake (*Elaphe obsoleta*). *J. Morphol.* **197**, 159–181. (doi:10.1002/jmor.1051970204)

66. Proske U. 1969 Vibration-sensitive mechanoreceptors in snake skin. *Exp. Neurol.* **23**, 187–194. (doi:10.1016/0014-4886(69)90055-7)

67. Roberts SF, Koditschek DE. 2019 Mechanical and virtual compliance for robot locomotion in a compliant world.

68. Li C, Pullin AO, Haldane DW, Lam HK, Fearing RS, Full RJ. 2015 Terradynamically streamlined shapes in animals and robots enhance traversability through densely cluttered terrain. *Bioinspiration \& biomimetics* **10**, 046003. (doi:10.1088/1748-3190/10/4/046003)

69. Gart SW, Li C. 2018 Body-terrain interaction affects large bump traversal of insects and legged robots. *Bioinspiration \& biomimetics* **13**, 026005.

70. Han Y, Wang Z, Li C. 2017 Body shape helps legged robots climb and turn in complex 3-D

terrains. In *APS Meeting Abstracts*,

71. Byl K, Tedrake R. 2009 Metastable walking machines. *Int. J. Rob. Res.* **28**, 1040–1064. (doi:10.1177/0278364909340446)
72. Othayoth R, Thoms G, Li C. 2019 Animals and robots vibrate to explore locomotion energy landscapes to make locomotor transitions. In *INTEGRATIVE AND COMPARATIVE BIOLOGY*, pp. E175–E175.
73. Garrido-Jurado S, Muñoz-Salinas R, Madrid-Cuevas FJ, Marín-Jiménez MJ. 2014 Automatic generation and detection of highly reliable fiducial markers under occlusion. *Pattern Recognit.* **47**, 2280–2292. (doi:10.1016/j.patcog.2014.01.005)
74. Crall JD, Gravish N, Mountcastle AM, Combes SA. 2015 BEEtag: A low-cost, image-based tracking system for the study of animal behavior and locomotion. *PLoS One* **10**, 1–13. (doi:10.1371/journal.pone.0136487)
75. Hedrick TL. 2008 Software techniques for two- and three-dimensional kinematic measurements of biological and biomimetic systems. *Bioinspiration and Biomimetics* **3**. (doi:10.1088/1748-3182/3/3/034001)
76. McDonald JH. 2014 *Handbook of Biological Statistics.*, 3rd edn. (Sparky House Publishing: Baltimore, MD.).

Supplementary Material

Materials and Methods

Robot parts

The robot was actuated with 19 Dynamixel XM430-W350-R servo motors operating at 14 V, powered by an external DC power supply (TekPower, CA, USA). The rubber O-rings wrapping each wheel were oil-resistant soft buna-n O-rings with an outer diameter of 48.1 mm and a width of 5.3 mm (McMaster-Carr, Elmhurst, IL, USA). The springs used in the suspension were compression springs with a length of 9.5 mm and an outer diameter of 3.1 mm (McMaster-Carr, Elmhurst, IL, USA). The maximal compression of each spring was 5 mm, which, when amplified by the lever arm (Fig. 2, red), limited the suspension deformation of each wheel to within 10 mm.

Large step obstacle track

We constructed a 180 cm long, 120 cm wide obstacle track using extruded T-slotted aluminum and acrylic sheets (McMaster-Carr, Elmhurst, IL, USA) (Fig. S1A). The step spanned the entire width of the track. To reduce slipping of the robot, we covered the horizontal surfaces of the step with a high friction rubber sheet (EPDM 60A 1.6 mm thick rubber sheet, Rubber-Cal, CA, USA).

Friction measurement

In friction experiments, we measured the position as a function of time of three body segments being dragged by a weight, by tracking ArUco tags in videos captured by Logitech C920 webcam at 30 frames/s. Then, by fitting a quadratic function of displacement as a function of time to estimate acceleration, we calculated kinetic friction coefficient as:

$$\mu = \frac{m_2 g - (m_1 + m_2)a}{m_1 g}$$

where m_1 is the mass of the weight, m_2 is the total mass of the segments, a is the fitted acceleration, g is the local gravitational acceleration (9.81514 m/s²).

Motor actuation to achieve partitioned gait

The actuation profile of yaw joints in the laterally undulating body sections, defined as the angular displacement from the straight body pose (Fig. 2B, yellow angle) as a function of time and segment index, followed the serpenoid gait [18]:

$$\theta_i = \begin{cases} A \sin(\omega t + \phi + (i-1)\Delta\phi), & i = 1, 2, \dots, k_1 \\ A \sin(\omega t + \phi + (i + k_1 - k_2)\Delta\phi), & i = k_2, \dots, 9 \end{cases}$$

where i is for the i th yaw joint from the robot head, $A = \pi/6$ and $\omega = \pi/2$ are the amplitude and angular velocity of each yaw joint angle waveform, $\phi = 0$ is the initial phase (at time zero) of the first yaw joint, and $\Delta\phi = -\pi/4$ is the phase difference between adjacent yaw joints. $\Delta\phi$ determines the wavenumber of the entire serpenoid wave in the robot, $k = 9|\Delta\phi|/2\pi$. The k_1 th yaw joint is the last yaw joint in the undulating section above the step, and the k_2 th yaw joint is the first yaw joint in the undulating section below the step, $k_2 - k_1$ is the number of pitch segments in the cantilevering section. The pitch angles of all pitch segments in these two undulating sections were set to zero (Fig. S2A, gray) to maintain contact with the horizontal surfaces.

The actuation profile of the joints of the cantilevering section (Fig. S2A, red) was designed to bridge across the large step with the minimal number of segments necessary. The yaw angles of all yaw segments in this section were set to zero. The pitch angle of the most anterior pitch joint in the undulating section below (Fig. S2A, joint c) was set to its maximal possible value ϕ_{\max} so that the cantilevering section was as vertical as possible to minimize cantilevering length. The two most anterior pitch joints in the cantilevering section (Fig. S2A, joints a and b) were set to keep the section above in contact with the upper horizontal surface. Their pitch angles were calculated as follows: $\phi_a = \phi_b - \phi_{\max}$, $\phi_b = -\sin^{-1}[(H -$

$n \text{hsin}\phi_{\max}/L]$, $n = \text{floor}[H/(\text{hsin}\phi_{\max})]$, where H is step height, h is the distance between two adjacent pitch axes when the robot is straight, n the maximum number of pitch and yaw segments that can be kept straight in the cantilevering section.

Marker-based feedback logic control

For feedback logic control [40] of the robot, a 3×3 cm ArUco marker [73] was fixed to the top of each pitch segment and on both the upper and lower horizontal surfaces near the top and bottom edge of the step (Fig. S1B). Their positions captured by a camera were tracked before each trial to measure the step height for adjusting the robot gait and then tracked online to locate the position of each pitch segment relative to the step. We used a webcam (C920, Logitech, Lausanne, Switzerland) with 1920×1080 resolution for experiments with step height $H \leq 38\% L$. We used another camera (Flea3, FLIR, OR, USA) with 1280×1024 resolution and a 12.5 mm lens (Fujinon CF12.5HA-1, Fujifilm, Minato, Japan) for experiments with $H > 38\% L$ because the webcam could not capture the entire setup with its limited focus length and angle of view.

The snake robot was controlled by a custom Robot Operating System (ROS) package running on an Ubuntu laptop connected with the online camera and a power sensor system to measure electrical power consumption (see below) (Fig. S2B). The laptop sent joint position commands to the servo motors and received motor angle readings at around 20 Hz. The online camera sent images to the laptop for online tracking of the ArUco markers at 20 Hz.

The feedback logic control algorithm is shown in flow chart (Fig. S2C). Before entering the main loop of online servo motor control at 25 Hz (in ROS time), the actuation profile of pitch segments was first calculated based on the step height acquired. In each control loop, the controller determined whether section division needed to be propagated down the body by checking: (1) whether the middle point of the motor axle line segment of the most posterior pitch segment in the cantilevering section had crossed a vertical plane 4 cm before and parallel to the vertical surface of the step but was no higher than 10 cm above the upper horizontal surface; or (2) whether the middle point of the motor axle line segment of the most anterior

pitch segment in the undulating section below the step had crossed a vertical plane 12 cm before and parallel to the vertical surface of the step. If either was true, the controller calculated the updated joint angles and sent angle commands to the servo motors. The controller continued this loop until a termination signal sent by the experimenter was received.

Electrical power measurement

We used two current sensors (Adafruit, NY, USA) between the servo motors and the power supply to record both voltage and current and measure electrical power of the robot (Fig. S3) at 100-135 Hz. The two sensors were installed on the power cord near the power supply in parallel to accommodate the large current drawn. The DC current and voltage data were sent to the laptop for recording with timestamps via an Arduino-based Single Chip Processor (SCP) communicating with the laptop.

Data synchronization

To synchronize motor angle data and electrical power data recorded by the laptop with the high-speed camera videos recorded on a desktop server, the power measurement circuit included a switch to turn on/off an LED bulb placed in the field of view of the high-speed cameras. When the LED was switched on/off, the SCP detected the voltage increase/drop and began/stopped recording power data. By aligning the initial and final power data points with the LED on/off frames in the videos and interpolating the motor position and electrical power data to the same sampling frequency as high-speed video frame rate (100 Hz), these data were synchronized.

Experiment protocol

At the beginning of each trial, we placed the robot on the surface below the step at the same initial position and orientation. The robot was set straight with its body longitudinal axis perpendicular to the vertical surface of the step. Its distance was set to be 16.5 cm from the wheel axle of the first segment to the vertical surface. This distance was selected so that the forward direction of most anterior segment in the

undulating section below the step was perpendicular to the vertical surface before it began to cantilever. We then started high-speed video recording and switched on the LED in the SCP circuit. Next, we started the robot motion and monitored traversal progress until a termination condition was met. After the robot motion was terminated, the LED was first switched off, then the high-speed camera recording was stopped, and the setup was reset for the next trial while high speed videos were saved.

3-D kinematics reconstruction

To reconstruct 3-D kinematics of the entire robot traversing the large step obstacle, we recorded the experiments using twelve high-speed cameras (Adimec, Eindhoven, Netherlands) with a resolution of 2592×2048 pixels at 100 frames s^{-1} (Fig. S1A). The experiment arena was illuminated by four 500 W halogen lamps and four LED lights placed from the top and side.

To calibrate the cameras over the entire working space for 3-D reconstruction, we built a three section, step-like calibration object using T-slotted aluminum and Lego Duplo bricks (The Lego Group, Denmark). The calibration object consisted of 23 landmarks with 83 BEEtags [74] facing different directions for automatic tracking. We then used the tracked 2-D coordinates of the BEEtag center points for 3-D calibration using Direct Linear Transformation (DLT) [75]. To obtain 3-D kinematics of the robot relative to the step, we used the 10 ArUco markers attached to the robot (one on each pitch segment), the two attached near the top and bottom edge of the step, and 13 additional ones temporarily placed on the three step surfaces before the first trial of each step height treatment. After all the experiments, we used a custom C++ script to track the 2-D coordinates of the corner points of each ArUco marker in each camera view. We checked and rejected ArUco tracking data whose four marker corners did not form a square shape with a small tolerance (10% side length).

Using the tracked 2-D coordinates from multiple camera views, we obtained 3-D coordinates of each tracked marker via DLT using a custom MATLAB script. We rejected marker data where there was an unrealistic large acceleration ($> 10 \text{ m/s}^2$), resulting from a marker suddenly disappearing in one camera view while appearing in another in the same frame. We then obtained 3-D position and orientation of each

pitch segment by offsetting its marker 3-D position and orientation using the 3-D transformation matrices from the marker to the segment, which was measured from the CAD model of the robot. We also measured the step geometry by fitting a plane to the markers on each of its three surfaces and generated a point cloud using the fit equation and the dimension of the three surfaces.

For yaw segments without markers and the pitch segments whose markers were not tracked due to occlusions or large rotation, we inferred their 3-D positions and orientations using kinematic constraints. We first tried inputting motor angles recorded by these segment motors into the robot forward kinematics to solve for their transformation matrices from other reconstructed segments. If their motor angles were not properly recorded, we tried inferring their positions and orientations from the two adjacent segments (as long as they were reconstructed). To do so, we first obtained all servo motor angles in this missing section by solving an inverse kinematics problem, then derived the transformation matrices of the missing segments from the forward kinematics. Finally, if both methods failed, we interpolated temporally from adjacent frames to fill in the missing transformation matrices. The interpolation was linearly applied on the twists of transformation matrices. We compared joint angles from the reconstructed segments to motor position data and rejected those with an error larger than 10° . To reduce high frequency tracking noise, we applied a window average filter temporally (*smooth2a*, averaging over 11 frames) to the 3-D positions of each segment after reconstructing all segments.

We verified the fidelity of 3-D kinematics reconstruction by projecting reconstruction back onto the high-speed videos and visually examined the match (Fig. S1B). The thresholds used in this process were selected by trial and error, with the aim of removing substantial visible projection errors while rejecting as few data as possible.

Data analysis

To quantify traversal performance, we measured traversal probability defined as the ratio of the number of trials in which the entire robot reached the surface above the step to the total number of trials for each step height. To quantify roll instability, we measured roll failure (flipping over) probability, defined

as the ratio of the number of failed trials in which the robot flipped over due to rolling to the total number of trials for each step height. To determine whether a wheel contacted a surface, we examined whether any point in the wheel point cloud (Fig. 8B, grey dashed circle) penetrated the surface assuming no suspension compression. Unrealistic body deformation values from tracking errors larger than the 10 mm limit from the mechanical structure were set to 10 mm.

To compare electrical power during traversal across step height and body compliance treatments, we analyzed electrical power over the traversal process, defined as from when the first pitch segment lifted to cantilever, to when the last pitch segment crossed the top edge of the step for successful trials, or to when the robot flipped over (roll failure) or the trial was terminated due to robot getting stuck (stuck failure) for failed trials.

To compare traversal performance of our robot with previous snake robots and the kingsnake, we calculated vertical traversal speed for each robot and the animal. For our snake robot and the kingsnake with multiple trials, we first calculated vertical traversal speed of each trial by dividing step height normalized to body length by traversal time and then pooled speed data of all trials from all step heights for each body compliance treatments (for the robot) to obtain average speed. The slopes shown in Fig. 9 are average vertical traversal speed for each robot and the animal.

During experiments, we rejected trials in which the robot moved out of the obstacle track before successfully traversing the step or failing to traverse due to occasional crash of the control program. We collected around 10 trials for each combination of step height and suspension setting (rigid and compliant). For the rigid body, 40% L step treatment only 5 trials were collected, because the 3-D printed segment connectors were often damaged by ground collisions during roll failure (flipping over) and had to be replaced. Detailed sample size is shown in Table S1.

Table S1. Sample size.

	$H = 31\% L$	$H = 36\% L$	$H = 38\% L$	$H = 40\% L$
Rigid	10	8	10	5
Compliant	10	11	10	10

Records of traversal success and roll failure (flipping over) were binomial values (1 for success and 0 for failure) for each trial and averaged across trials to obtain their probabilities for each step height and body compliance treatment. For each trial, contact probability, body deformation, and surface conformation difference were averaged spatiotemporally over time and across all pitch segments in the undulating sections above and below the step combined. Electrical power was averaged over time for each trial. Finally, these trial averages were further averaged across trials for each step height and body compliance treatment to obtain treatment means and standard deviations (s.d.) or confidence intervals, which are reported in figures.

Statistics

To test whether traversal probability and roll failure (flipping over) probability depended on step height, for the rigid or compliant body robot, we used a simple logistic regression separately for each of these measurements, with step height as a continuous independent factor and records of traversal success or roll failure (flipping over) as a nominal dependent factor.

To test whether traversal probability and roll failure (flipping over) probability further depended on body compliance while taking into account the effect of step height, we used a multiple logistic regression for each of these measurements with data from rigid and compliant body robot combined, with body compliance as a nominal independent factor and step height as a continuous independent factor and records of traversal success or roll failure (flipping over) as a nominal dependent factor.

To test whether traversal probability differed between each adjacent pair of step heights for the rigid or compliant body robot, we used a pairwise chi-square test for each pair of step heights, with step height as a nominal independent factor and traversal success record as a nominal dependent factor.

To test whether contact probability, body deformation, surface conformation difference, and electrical power differed between rigid and compliant body robot, we used an ANCOVA for each of these measurements. We first set body compliance, step height, and their interaction term as independent factors

and each of these measurements as a nominal/continuous dependent factor. If the P value of the interaction term was less than 0.05, we then re-ran the same test excluding the interaction term.

To test whether vertical traversal speed differed between rigid and compliant body robot and the kingsnake, we used a two-sample t -test for each pair of the three subjects, with the subject as a nominal independent factor and vertical traversal speed as a continuous dependent factor.

All the statistical tests followed the SAS examples in [76] and were performed using JMP Pro 13 (SAS Institute, Cary, NC, USA).

Supplementary Figures

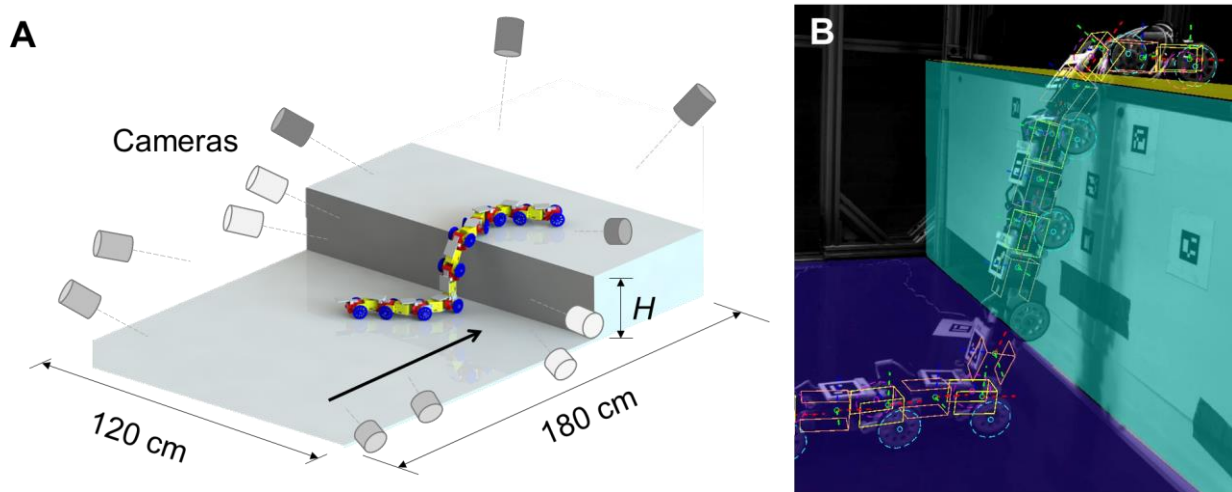


Fig. S1. Experimental setup and 3-D kinematics reconstruction. (A) Schematic of experimental setup.

Twelve high-speed cameras are used for 3-D kinematics reconstruction, divided into groups of four (different shades) focusing on three step surfaces. (B) High-speed video snapshot of robot traversing step, with projection of reconstructed body segments, wheels, and step surfaces. Yellow and orange boxes are reconstructed yaw and pitch servo motors. Dashed magenta and cyan circles are reconstructed left and right wheels assuming no suspension compression. Violet, cyan, and gold surfaces are reconstructed lower horizontal, vertical, and upper horizontal surfaces.

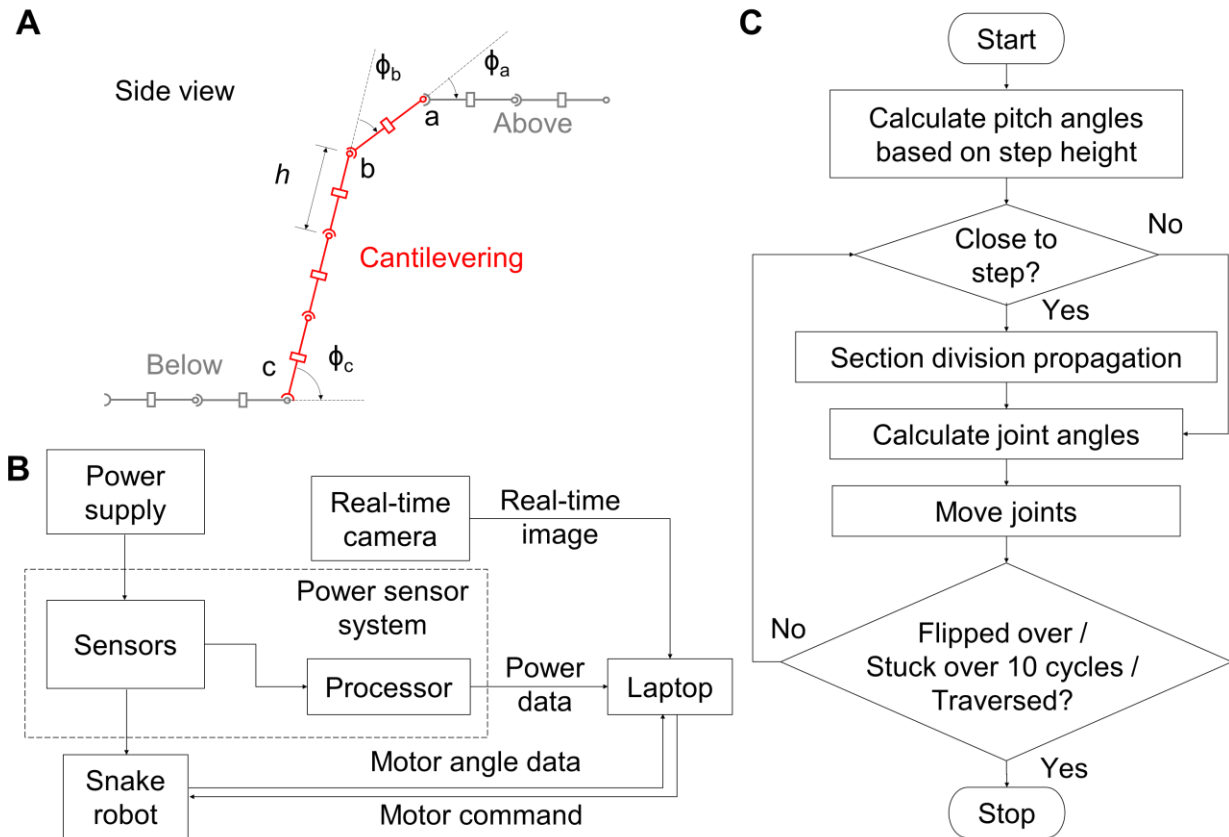


Fig. S2. Controller design. (A) Side view schematic of partitioned gait design to show control of cantilevering section (red). Three pitch angles are calculated based on measured step height, including: ϕ_a and ϕ_b of the two most anterior pitch joint of the cantilevering section and ϕ_c of the most anterior pitch joint of the undulating section below the step. (B) Data acquisition system. (C) Flow chart of robot control. For (B) and (C), see **Section 2.2** in main text and **Marker-based feedback logic control** and **Electrical power measurement** in Materials and Methods for detailed description.

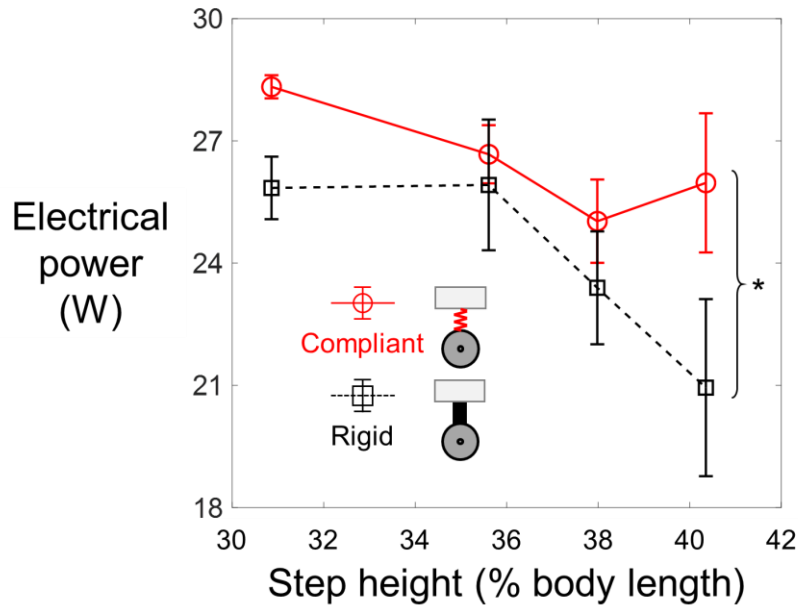


Fig. S3. Effect of body compliance on electrical power. Electrical power of robot as a function of step height. Black dashed is for rigid body robot; red solid is for compliant body robot. Error bars show ± 1 s.d. Bracket and asterisk represent a significant difference between rigid and compliant body robot ($P < 0.0001$, ANCOVA).

Supplementary Movies

Movie 1. [Snake robot uses a snake-like partitioned gait to traverse a large step rapidly.](#)

Movie 2. [Flipping over of a snake robot when traversing a large step.](#)

Movie 3. [Adding body compliance to a snake robot.](#)

Movie 4. [Comparison of large step traversal between rigid and compliant body snake robot.](#)